




Statics and dynamics of drops spreading on a liquid-liquid interface

Madhurima Reddy , Manivannan M, Madivala G. Basavaraj , and Sumesh P. Thampi ^{*}
Department of Chemical Engineering, Indian Institute of Technology Madras, Chennai 600036, India



(Received 29 April 2020; accepted 1 October 2020; published 26 October 2020)

The spreading of drops on surfaces is ubiquitous and has relevance to many technological applications. In this work, we present two-dimensional numerical simulations of the surface tension driven spreading of drops dispensed on a fluid-fluid interface. A comprehensive picture describing the equilibrium shapes of the drops is provided in the form of a state diagram. We show that the analysis of kinetics of drops that spread symmetrically on the fluid-fluid interface reveal several interesting features: (i) the existence of a single length scale that describes the spreading process, (ii) the power law dependence of the temporal variation of the geometrical parameters of the spreading drop, (iii) the linear dependence of the power law exponents on the equilibrium enclosing angle of the liquid drop, (iv) a strong dependence of the power law exponents on the spreading coefficient, and (v) a collapse of the spreading kinetics data into a master curve. Though restricted to two dimensions, our analysis provides a rationale for explaining experimentally determined power law exponents which have been reported to vary over a wide range and hence to understand the universal nature of the spreading process.

DOI: [10.1103/PhysRevFluids.5.104006](https://doi.org/10.1103/PhysRevFluids.5.104006)

I. INTRODUCTION

Spreading of a miscible or immiscible fluid on a fluid-fluid interface is a process often encountered in several disciplines of science and engineering. Some of the novel applications of such a phenomena are (i) spreading of an active pharmaceutical ingredient on the interface of the air and liquid lining in the lung for the treatment of pulmonary infections [1], (ii) development of liquid lens based imaging devices as alternatives to the conventional optical lenses [2], (iii) oil drop test (Taila Bindu pariksha) as a cost effective disease diagnostic tool which involves spreading of oil drops on human urine samples [3,4], and (iv) the fate, transport, and remediation of oil spills on the sea water surface [5]. The efficacy of processes involving spreading of liquids on fluid-fluid interfaces requires a systematic study of the statics of droplets and the dynamics of spreading.

The rate of spreading measured experimentally for various combinations of miscible and immiscible fluids generally follows a power law of the form $R(t) \propto t^{\mu}$. Such a power law behavior arises from the interplay between various forces originating due to gravity, inertia, viscosity, and surface tension. For the drops dispensed on liquid substrates, with both liquids being nonvolatile and immiscible, a balance of viscous and surface tension force reveals that the spreading proceeds as [6]

$$R(t) \sim \left(\frac{\gamma V^2 L}{\mu} \right)^{\frac{1}{8}} t^{\frac{1}{8}}, \quad (1)$$

where γ is the surface tension force that is driving the spreading process, and V is the volume of the drop that is spreading on a liquid substrate of height L and viscosity μ . On the other hand, different

^{*}sumesh@iitm.ac.in

values of n_R are also reported in this spreading regime, for example, when the height of the substrate liquid is much larger (i.e., deep liquid substrate) such that the solid boundaries that contain the liquid do not influence the spreading behavior of the drop, the radial spreading rate dictated by a balance of surface tension and viscous forces is given by [5,7,8]

$$R(t) = K \frac{S^{1/2}}{(\rho\mu)^{1/4}} t^{3/4}, \quad (2)$$

where μ and ρ are the viscosity and the density of substrate liquid, respectively. S is the spreading coefficient (which will be defined later) and K is a constant, the value of which depends upon the geometry of the spreading phase [9]. As the relative importance of the forces during the course of spreading change, time-dependent power law exponents can capture the evolving spreading dynamics. In the spreading of oil spills on the sea, Hoult [5] proposed that in the early stages of spreading, the inertial and gravitational forces balance each other, giving rise to $R(t) \sim t^{1/2}$. In the second stage, as the gravitational and the viscous forces balance each other, the spreading continues again with the scaling $R(t) \sim t^{1/2}$. The spreading in the final stage is governed by a balance between the viscous and the surface tension forces, which gives the scaling law $R(t) \sim t^{3/4}$ [7,10–12].

Clearly, different scaling laws give widely different exponents depending on the spreading regime. Experiments also present a similar situation. For example, the exponent $n_R \approx \frac{1}{8}$ has been observed in the experiments of Fraaije and Cazabat [13], where silicone oils of different viscosity are spread on a glycerine-water mixture. Silicone oil of various viscosities spreading unidirectionally on the surface of water taken in a rectangular container is shown to spread with power law exponent $n_R = \frac{3}{4}$ [14]. Similar power law dependence is observed after studying spreading of oleic acid on water surfaces [15]. The $t^{3/4}$ scaling has also been observed for the spreading of a monolayer of polydimethylsiloxane (PDMS) oil on a surfactant laden aqueous phase [16]. The investigation of spreading of immiscible volatile liquids on pure water by laser shadowgraphy revealed that the leading edge of the spreading drop follows a $n_R = \frac{1}{2}$ power law with respect to time instead of $n_R = \frac{3}{4}$ [17]. The $n_R = \frac{1}{2}$ and $n_R = \frac{1}{4}$ power law exponents have been observed in spreading of miscible liquids on pure liquids [18,19]. The spreading exponent is also found to depend on the geometry of the leading edge, that is, planar front or axisymmetric [7]. Another parameter that influences the spreading rate is the thickness of the substrate liquid [13]. If a small volume of substrate liquid is considered such that the thickness of the substrate liquid is small, then spreading occurs on a thin layer of liquid. The spreading exponent in such cases can be as low as $n_R = 0.1$ due to the influence of the solid surface beneath the substrate liquid [18]. Therefore, the spreading is drastically hindered, and n_R is closer to the predictions by Tanner's law on solid substrates [20].

Considering a large variation in the exponent n_R , which is attributed to various factors such as (i) miscibility of the fluids and their volatility, (ii) geometry of the spreading front, and (iii) the height and properties of substrate fluid, a one to one correspondence between theoretical predictions and experimental observations will remain inconclusive, and warrants a systematic investigation of the spreading behavior in a controlled environment. The experiments on spreading of fluid on a fluid-fluid interface are further complicated, as it is affected by several external factors such as the height of release of the drop and the consequent impact, the interface undulations due to vibration, choice of available liquids, etc. On the other hand, controlled spreading experiments can be achieved in numerical simulations, the main theme of this article. We focus on a systematic investigation of the spreading regime governed by surface tension–viscous force balance and establish the unexpected role of surface tension forces on the power law exponents. In this work, we only change the interfacial tension between the fluids (namely, the spreading coefficient) and do not change any other fluid properties or external forces such as gravity, thus isolating the effects of interfacial tension forces alone on the drop spreading kinetics.

The numerical simulation of spreading of drops on a fluid-fluid interface is also equally daunting. This is because of the presence of multiple fluid-fluid interfaces which continuously evolve and are also accompanied by fluid flows. Therefore, the numerical solutions are not only solutions of

governing equations which are nonlinear partial differential equations, they also involve interface tracking. Hence, most of the theoretical and simulation studies have been for systems with spreading coefficient $S > 1$, wherein the lubrication approximation has been exploited considering that a spreading drop forms a thin liquid film over the fluid-fluid interface [12–15,21,22]. Surprisingly, many of the experimental studies and theoretical developments of spreading in such ternary systems in literature are a few decades old [5,6,10,11,13,14].

In this article, we use a hybrid lattice Boltzmann (LB) algorithm, an efficient technique for simulating mesoscale systems along with a diffuse interface model which facilitates determining the temporal evolution of the interface without explicit tracking. We investigate the statics of drops on liquid-liquid interfaces and the dynamics of spreading by carrying out two-dimensional (2D) simulations. In order to systematically investigate the scaling behavior associated with the spreading process, we consider a system of three immiscible liquids of equal density and viscosity, initialized by placing a circular drop on the liquid-liquid interface. In such systems the spreading is solely driven by surface tension forces, and the contribution to viscous dissipation from all the fluids is the same. Our numerical simulations show that the temporal evolution of all the geometrical parameters that characterize the spreading drop follow a three stage process where the intermediate stage exhibits a power law behavior in the thin film limit. The relation between the power law exponents show that the spreading kinetics can be described by a single length scale. Our analysis, though restricted to two dimensions, provides a rationale for explaining widely varying experimentally determined power law exponents. Finally, we present a master curve that collapses the spreading kinetics data of drops of different equilibrium enclosing angles.

The article is organized as follows: In Sec. II we describe the governing equations, the simulation methodology, and the scaling analysis associated with drops spreading in two and three dimensions. The equilibrium shapes of the drop on the liquid-liquid interface are analyzed in Sec. III A, and the results are presented in the form of a state diagram. In Sec. III B, the analysis of kinetics of drops that spread symmetrically on the fluid-fluid interface is discussed.

II. GOVERNING EQUATIONS AND METHODOLOGY

The interface between any two immiscible fluids is characterized by change in any physical and/or chemical properties when traversed perpendicular to the interface. In a nonequilibrium process such as spreading of a drop, the interfaces continuously evolve until the system reaches an equilibrium state. This process can be described using a diffuse interface model as discussed below.

A. Diffuse interface model for a drop spreading on a fluid-fluid interface

Consider a fluid-fluid interface formed by fluid 1 and fluid 2 on which a drop of fluid 3 is spreading as shown in Fig. 1(a). The fluids considered—fluids 1, 2, and 3—are immiscible with each other. The free energy of such a ternary fluid system, occupying a volume Ω , can be written as [23–25]

$$F = \int_{\Omega} \left[\frac{k_1}{2} C_1^2 (1 - C_1)^2 + \frac{k_2}{2} C_2^2 (1 - C_2)^2 + \frac{k_3}{2} C_3^2 (1 - C_3)^2 + \frac{k'_1}{2} (\nabla C_1)^2 + \frac{k'_2}{2} (\nabla C_2)^2 + \frac{k'_3}{2} (\nabla C_3)^2 \right] d\Omega, \quad (3)$$

where C_1 , C_2 , and C_3 correspond to the mass density of fluids 1, 2, and 3. While the first three terms in Eq. (3) correspond to the bulk free energy, the last three terms correspond to the contribution of energy due to the presence of interfaces [26]. The constants k_m and k'_m respectively determine the strength of bulk and interfacial contributions to the total free energy due to the fluid component m . These constants are related to the interfacial thickness and interfacial tensions between the fluids.

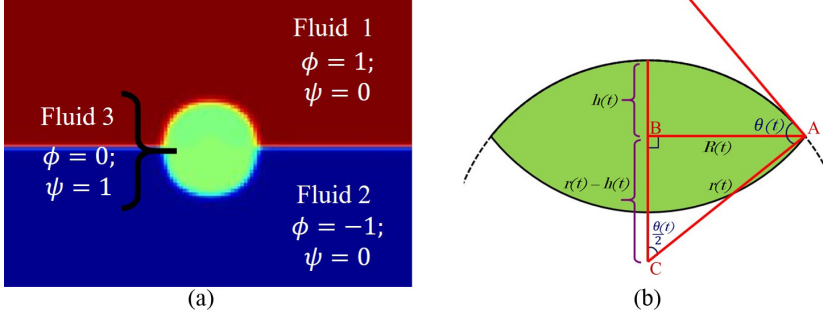


FIG. 1. (a) Initial configuration of ternary fluid system in the simulations, wherein a drop of fluid 3 is placed on a fluid 1–fluid 2 interface. (b) A schematic of the lens formed at any time t during the spreading of fluid 3 on the fluid 1–fluid 2 interface. Assuming the lens to be part of a circle of radius $r(t)$, the geometrical construction that uses the radius $R(t)$, the height $h(t)$ of the lens to determine the enclosing angle $\theta(t)$ is shown.

The interfacial thickness between two fluids m and n is given by [24]

$$w_{mn} = \sqrt{\frac{k'_m + k'_n}{k_m + k_n}} \quad (4)$$

and the interfacial tension by

$$\gamma_{mn} = \frac{\sqrt{(k'_m + k'_n)(k_m + k_n)}}{6} = \frac{w_{mn}}{6}(k_m + k_n). \quad (5)$$

Note that the values of k_m and k'_m must be positive for all three fluids to be immiscible with each other. Since $C_1 + C_2 + C_3 = \rho$, the total mass density of the ternary fluid system is fixed and initialized to be 1, we only need two quantities to describe the concentration field and hence we define two order parameters: $\phi = C_1 - C_2$ and $\psi = C_3$. In pure fluid 1, $C_1 = 1$ and $C_2 = C_3 = 0$; therefore, $\phi = 1$ and $\psi = 0$. Similarly, in pure fluid 2, $\phi = -1$ and $\psi = 0$ while in pure fluid 3, $\phi = 0$ and $\psi = 1$. Therefore both ϕ and ψ together can be used to identify the three different fluids in the ternary system [24].

Cahn-Hilliard equations describe the spatial and temporal evolution of the order parameters ϕ and ψ and are given by [27,28]

$$\frac{\partial \phi}{\partial t} + \nabla \cdot (\phi \mathbf{v}) = M_\phi \nabla^2 \mu_\phi, \quad (6)$$

$$\frac{\partial \psi}{\partial t} + \nabla \cdot (\psi \mathbf{v}) = M_\psi \nabla^2 \mu_\psi, \quad (7)$$

where \mathbf{v} is the fluid velocity field, $\mu_\phi = \delta F / \delta \phi$ is the chemical potential field for the order parameter ϕ , $\mu_\psi = \delta F / \delta \psi$ is the chemical potential field for the order parameter ψ , and M_ϕ and M_ψ are the mobility parameters. These equations involving the unsteady (first term), advective (second term), and the diffusive (term on the right hand side) contributions represent the conservation of the two order parameters.

The evolution of the velocity field during spreading is described by continuity and Navier-Stokes equations [26,29]:

$$\nabla \cdot \mathbf{v} = 0, \quad (8)$$

$$\rho \left[\frac{\partial \mathbf{v}}{\partial t} + \mathbf{v} \cdot \nabla \mathbf{v} \right] = -\nabla p + \eta \nabla \cdot (\nabla \mathbf{v} + \nabla \mathbf{v}^T) - \rho \nabla \mu_\rho - \phi \nabla \mu_\phi - \psi \nabla \mu_\psi, \quad (9)$$

where p is the pressure field and η is the dynamic viscosity. The terms $\rho \nabla \mu_\rho$, $\phi \nabla \mu_\phi$ and $\psi \nabla \mu_\psi$ are the additional force density terms that arise due to the presence of the interfaces [24]. The effects due to interfacial tensions between the fluids are captured by incorporating these additional terms into the Navier-Stokes equations.

B. Simulations and analysis details

The governing equations are solved using a hybrid lattice Boltzmann method [30–32], which involves solving the Cahn-Hilliard equations [Eqs. (6) and (7)] using the method of lines and the Navier-Stokes equations [Eq. (9)] using a lattice Boltzmann algorithm. In the method of lines for Eqs. (6) and (7), the spatial derivatives are discretized using a central difference scheme, and the resulting set of ordinary differential equations are integrated numerically using the Runge-Kutta method. A single relaxation time lattice Boltzmann algorithm on a $D3Q15$ lattice is used for the simulations of Navier-Stokes equations. The spatial and temporal discretizations are chosen as unity, i.e., $\Delta x = 1$ and $\Delta t = 1$ for convenience [30,33,34]. The velocity field obtained from the lattice Boltzmann method is used in the advection term of Cahn-Hilliard equations, while the order parameter field is used to calculate the interfacial forces in the Navier-Stokes equations. Therefore Eqs. (6), (7), and (9) are solved in a coupled fashion to calculate the velocity and order parameter fields, thus enabling a complete description of the dynamics of a three fluid system, for example, to capture the behavior of a fluid drop spreading on a fluid-fluid interface.

Simulations are done in two dimensions by considering a square domain of 400×400 lattice units (l.u.). The simulations are initialized by placing a circular drop of diameter 30 l.u. as shown in Fig. 1(a). Periodic boundary conditions are applied on all domain boundaries. The dynamics of the spreading process is captured by following the simulation up to 10^6 time steps. In the simulations presented in the manuscript, w_{mn} is kept as a constant and k is changed to obtain different values of interfacial tensions [see Eq. (5)]. This allowed us to reduce the number of independent parameters that can be changed in the simulations. Moreover, the idea of introducing a finite interfacial width in the simulations is to obtain numerical stability of the algorithm. The same results reported in this work are expected irrespective of the value of w_{mn} . The parameter k_1 is varied from 0.0007 to 0.495, k_2 is fixed at 0.005, and k_3 is varied from 0.000 75 to 0.035 in the simulations to access a range of interfacial tensions but by maintaining the value of w_{mn} fixed at 0.4472 in all simulations, as typically used in diffuse interface simulations [30]. The mobility parameters M_ϕ and M_ψ are assumed to be same and are equal to 0.01. The density ($\rho = 1$) and viscosity ($\mu = 0.6667$) of all three fluids are also assumed to be same. Gravity is irrelevant in the simulations since the three fluids have the same density. Therefore the simulations capture the spreading behavior solely driven by surface tension.

The simulation results are analyzed using a customized code scripted in MATLAB. The instantaneous radius $R(t)$ and height $h(t)$ of the liquid lens of fluid 3 residing on the fluid 1–fluid 2 interface [see Fig. 1(b)] is determined at every time step to track the spreading process. The following algorithm was used for this purpose. As one traverses in the horizontal or vertical direction within the simulation box, a jump in the order parameter ψ occurs (from 0 to 1 or 1 to 0), indicating the existence of either a fluid 1–fluid 3 interface or a fluid 2–fluid 3 interface. Vertical and horizontal lines that intersect the lens formed by fluid 3 give rise to several chords. The maximum chord length in the horizontal direction is the diameter of the lens, $2R(t)$, and that in the vertical direction is the thickness of the lens, $2h(t)$.

The fluid 1–fluid 3 interface and fluid 2–fluid 3 interface intersect at the three-phase contact point, forming a vertex that encloses an angle θ [see Fig. 1(b)]. This angle, which evolves as spreading proceeds, can be determined as follows. We assume that the fluid 1–fluid 3 interface is part of a circle of radius $r(t)$ at any time instant t , as shown in Fig. 1(b). Since $h(t)$ and $R(t)$ are already determined, the radius of the circle $r(t)$ can be calculated by applying the Pythagoras theorem to Δ^{ABC} , which gives $r(t) = \frac{R(t)^2 + h(t)^2}{2h(t)}$. This enables the calculation of the enclosing angle $\theta(t)$ using the $\theta(t) = 2 \sin^{-1} \left(\frac{R(t)}{r(t)} \right)$.

C. Scaling analysis

Following Fraaije and Cazabat [13], we present a scaling analysis of a drop spreading in two dimensions. We can derive scaling laws in the limit of a small enclosing angle (contact angle). The driving force that leads to the spreading of the drop is the difference between the instantaneous (dynamic) enclosing angle (contact angle) $\theta(t)$ and the equilibrium enclosing angle θ_e . The surface tension force per unit length of the contact line is given by $F_s = \gamma[\cos \theta(t) - \cos \theta_e]$, where γ is the characteristic drop-fluid interfacial tension. In the limit of $\theta(t) \rightarrow 0$ and when $\theta_e = 0$, $F_s \sim \gamma\theta(t)^2$. Approximating the drop shape as a wedge, and for small angles, $\theta \sim \frac{h}{R}$.

Considering the drop as a thin film, the viscous force per unit length of the contact line can be estimated by multiplying the viscous stress with the contact radius as $F_v \sim \mu \frac{dv}{dy} R \sim \mu \frac{dR}{dt} \frac{R}{L}$, where L is the characteristic length scale over which viscous forces act. Since all three fluids considered in this work have the same viscosity, it is appropriate to consider L to be the thickness of the substrate liquid. Equating the expressions for F_s and F_v ,

$$\gamma \left(\frac{h}{R} \right)^2 \sim \mu \frac{dR}{dt} \frac{R}{L}. \quad (10)$$

For the spreading of drops in two dimensions, the area of the drop $A \sim Rh$ is conserved. Substituting for $h \sim \frac{A}{R}$ and integrating we get

$$R \sim \left(\frac{\gamma A^2 L}{\mu} \right)^{\frac{1}{6}} t^{\frac{1}{6}}. \quad (11)$$

In three dimensions, the volume of the drop $V \sim R^2 h$ is conserved. Substituting for $h \sim \frac{V}{R^2}$ we obtain

$$R \sim \left(\frac{\gamma V^2 L}{\mu} \right)^{\frac{1}{8}} t^{\frac{1}{8}}. \quad (12)$$

Thus the contact radius R follows a power law, $R \sim t^{n_R}$, with the power law exponent $n_R = \frac{1}{6}$ in two dimensions and $n_R = \frac{1}{8}$ in three dimensions.

Similarly, both the height of the drop (h) as well as the enclosing angle (θ) can be shown to follow a power law behavior, $h \sim t^{n_h}$ and $\theta \sim t^{n_\theta}$. Since $h \sim \frac{A}{R} \sim t^{-n_R}$ we obtain $n_h = -n_R$ in two dimensions. On the other hand, in three dimensions, $h \sim V/R^2$, implying $n_h = -2n_R$. However, $\theta \sim h/R$ in both two and three dimensions, and hence $n_\theta = n_R - n_h$.

III. RESULTS AND DISCUSSION

A. Comparison of simulation data with Neumann's relation

We first test the validity of the Neumann triangle relation for the data obtained from simulations. Figure 2 is a schematic of fluid 3 residing at the fluid 1–fluid 2 interface in which the surface tension forces at the three phase contact point are shown. The three surface tension forces balance each other at equilibrium such that the contact angles between any two interfaces satisfy the Neumann triangle relation,

$$\frac{\gamma_{12}}{\sin \theta_e} = \frac{\gamma_{23}}{\sin \alpha} = \frac{\gamma_{31}}{\sin \beta}, \quad (13)$$

where γ_{12} is the interfacial tension between fluid 1 and fluid 2, γ_{23} is the interfacial tension between fluid 2 and fluid 3, and γ_{31} is the interfacial tension between fluid 3 and fluid 1. α , β , and θ_e are the enclosing angles between the tangents drawn along the interfaces at the three phase contact point as marked Fig. 2. Equation (13) can be derived by applying the law of sines on the triangular construction with the angles $\pi - \alpha$, $\pi - \beta$ and $\pi - \theta_e$ and sides γ_{23} , γ_{31} , and γ_{12} shown in Fig. 2.

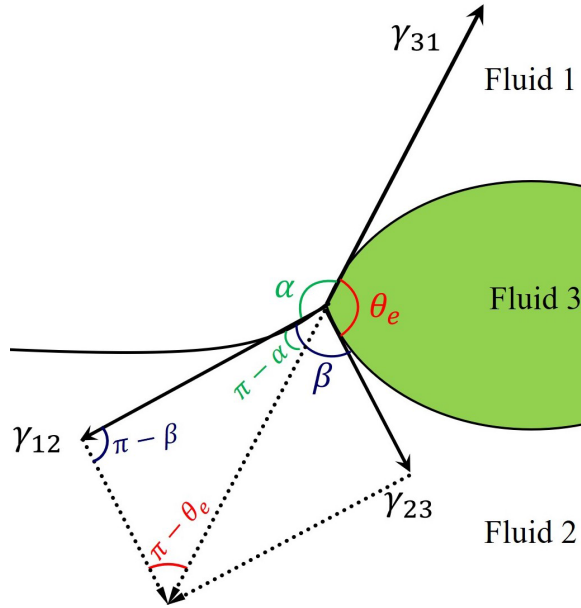


FIG. 2. A schematic representation of the three phase contact point formed by the intersection of lens of fluid 3 with the fluid 1–fluid 2 interface. The fluid combinations are such that the spreading coefficient, $S < 0$. The angles α , β , and θ_e marked in fluid 1, fluid 2, and fluid 3, respectively, are the angles that are enclosed between the tangents drawn at the three-phase contact point to the interfaces. The triangle with the angles $\pi - \alpha$, $\pi - \beta$, and $\pi - \theta_e$ and sides γ_{23} , γ_{31} , and γ_{12} can be used to obtain the Neumann relation using the law of sines.

The three surface tensions can be used to define a thermodynamic quantity S , called the spreading coefficient [35]:

$$S = \gamma_{12} - (\gamma_{23} + \gamma_{31}). \quad (14)$$

$S > 0$ indicates spontaneous spreading of fluid 3 on the interface of fluid 1 and fluid 2, while $S < 0$ leads to a stable lens shaped drop of fluid 3 at the interface of fluid 1 and fluid 2 [20].

In Fig. 3, the enclosing angle θ_e obtained from simulations corresponding to equilibrium drop shape is plotted against the theoretical value of θ_e calculated from the Neumann's relation [Eq. (13)]. As indicated by a line of slope 1, a good agreement of the enclosing angle obtained by the two methods validates the simulation methodology adopted here.

Since a ternary system involves three interfacial tensions, it is convenient to recast Eq. (14) by dividing both sides with γ_{12} to obtain

$$S^* = 1 - (a + b), \quad (15)$$

where $S^* = S/\gamma_{12}$ is the normalized spreading coefficient, $a = \gamma_{23}/\gamma_{12}$, and $b = \gamma_{31}/\gamma_{12}$. Similar to S , the normalized spreading coefficient S^* will only indicate if a drop of fluid 3 spreads on a fluid 1–fluid 2 interface or not. In other words, if $S^* > 0$ or equivalently, $(a + b) < 1$, this indicates spontaneous spreading of fluid 3 on the fluid 1–fluid 2 interface and vice versa. In this work simulations are performed for ternary fluid systems with $S^* < 0$.

While three interfacial tensions are required to uniquely specify the equilibrium shape of a drop, the above normalization also enables us to determine the drop shape in terms of just two parameters a and b , as described in the next section. Similarly, the dynamics of the spreading process also depend on these parameters a and b , which will be elaborated further. In the following we will first analyze the equilibrium shapes of the drops followed by spreading kinetics.

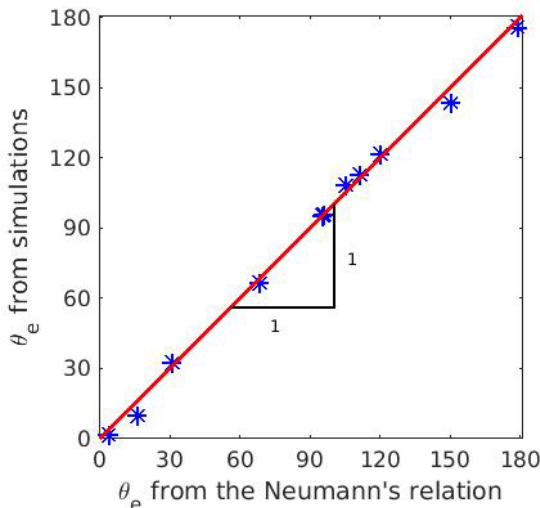


FIG. 3. Validation of the simulation methodology for the equilibrium drop shapes by comparing the theoretical and simulated equilibrium enclosing angles (θ_e) for various values of surface tensions γ_{12} , γ_{23} , and γ_{13} . A line of slope = 1 confirms a good match between the simulation results and those given by Neumann's relation.

B. Equilibrium shapes of the lens

In our simulations, the equilibrium shape of the drop corresponds to a state when the flow fields in the three fluids decay to zero and the total free energy of the system is minimum. Consequently, the radius $R(t)$ and height $h(t)$ reach a plateau when the lens assumes the equilibrium shape. Figure 4 shows the equilibrium shapes of the liquid lens formed at the fluid 1–fluid 2 interface for different values of a and b (indicated below each subfigure).

The top panel of Figs. 4(a)–4(d) shows the equilibrium shapes for the cases when $a = b$. The lens shapes are symmetric about the fluid 1–fluid 2 interface. Since $a = b$, the free energy associated with both the fluid 1–fluid 3 interface and fluid 2–fluid 3 interface are the same, which implies that the two interfacial areas must be the same, resulting in a symmetric shape. As the magnitude of a (or b) increases, the free energy associated with the two interfaces (fluid 1–fluid 3 and fluid 2–fluid 3) compared to the fluid 1–fluid 2 interface increases, and therefore the system minimizes the interfacial contact area, forming a lens of smaller radius and larger height. A further increase in a (or b) beyond 3 will result in a circular drop residing on the fluid 1–fluid 2 interface.

Next we consider the case where $a \neq b$. In such scenarios the drop shapes are not symmetric about the fluid 1–fluid 2 interface, as shown in the second panel [Figs. 4(e)–4(h)]. When $a > b$, fluid 3 prefers to reside in fluid 2, as shown in Figs. 4(e) and 4(f). However, when $a < b$, fluid 3 prefers to reside in fluid 1, as shown in Figs. 4(g) and 4(h). The condition $a < b$ means that $\gamma_{23} < \gamma_{31}$; therefore the system can afford to have a larger fluid 2–fluid 3 interfacial area and yet minimize the total free energy. This results in an asymmetric shape, with fluid 3 residing more in fluid 2 compared to fluid 1. The converse is true when $a > b$. As the magnitude of a and b are increased, the drop diameter decreases and the height increases. This is because the free energy associated with both fluid 1–fluid 3 and fluid 2–fluid 3 interfaces increases when compared to the fluid 1–fluid 2 interfacial free energy. The reduction in diameter of the lens can be noticed when the equilibrium drop shape shown in Fig. 4(e) is compared with that in Fig. 4(f) and the equilibrium drop shape shown in Fig. 4(g) is compared with Fig. 4(h). When the magnitudes of a and b are further increased, fluid 3 will assume the shape of a circular drop that will be completely immersed in either fluid 1 or fluid 2. An example of such a scenario is shown in Fig. 4(i) when $a = 0.5$ and

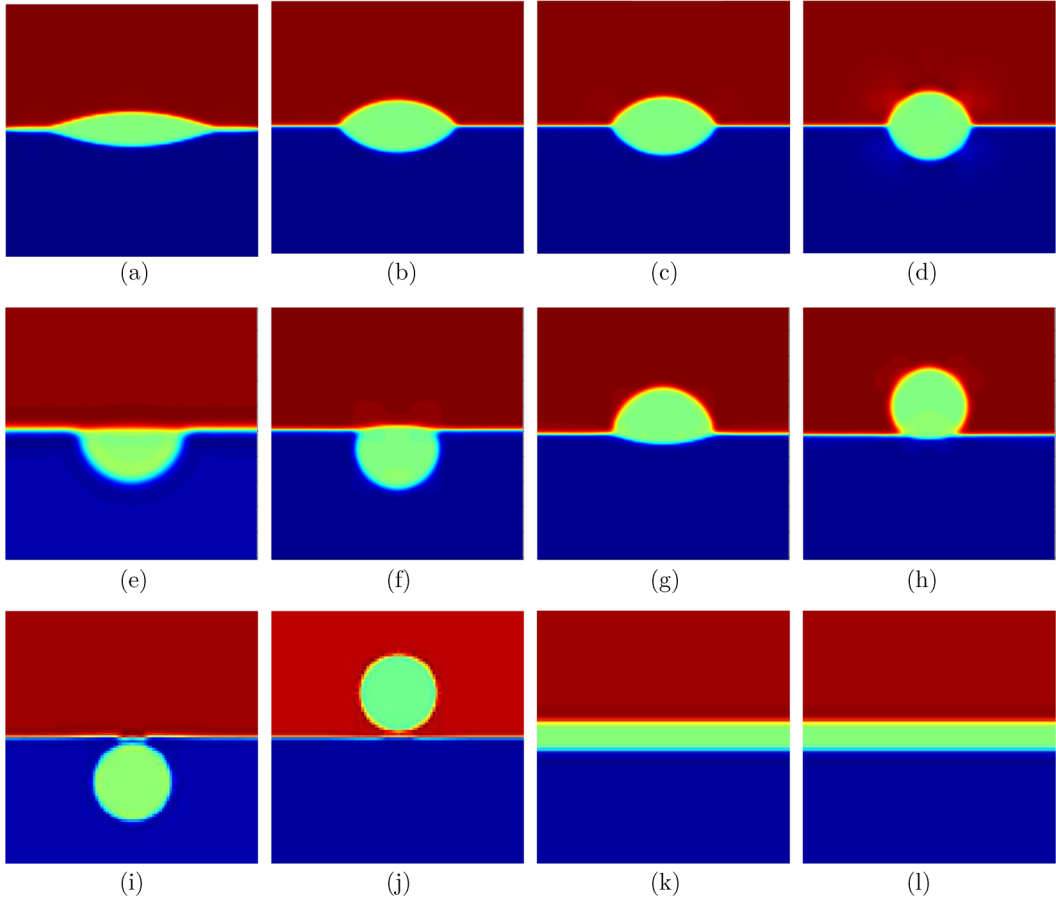


FIG. 4. The equilibrium configurations of fluid 3 drops placed on a fluid 1–fluid 2 interface for various values of a and b . The simulation results in (a)–(d) show symmetric lenses that correspond to the case $a = b$. The simulation results in (e)–(h) show asymmetric lenses corresponding to the case $a \neq b$. The configurations in (i) and (j) show that fluid 3 resides completely in fluid 2 and fluid 1, respectively. The spreading of fluid 3 into a thin film is shown in (k) and (l). (a) $a = b = 0.5$; (b) $a = b = 0.75$; (c) $a = b = 1$; (d) $a = b = 3$; (e) $a = 0.1, b = 1$; (f) $a = 0.5, b = 1.25$; (g) $a = 1, b = 0.5$; (h) $a = 2, b = 1.25$; (i) $a = 0.5, b = 2.75$; (j) $a = 2.5, b = 0.75$; (k) $a = 0.1, b = 0.8$; (l) $a = 0.5, b = 0.2$.

$b = 1.5$. The drop of fluid 3 prefers to exist solely in contact with fluid 2, since $a < b$. The converse situation is shown in Fig. 4(j) when $a = 2$ and $b = 1$.

When $(a + b) \leq 1$, then $S^* \geq 0$, indicating that a drop of fluid 3 placed on the fluid 1–fluid 2 interface spreads completely, forming a thin film. This situation, which occurs irrespective of magnitudes of a and b as long as $(a + b) \leq 1$, is illustrated in Figs. 4(k) and 4(l).

The equilibrium shapes that the fluid 3 placed on the fluid 1–fluid 2 interface adopts depending upon the values of a and b can be comprehensively represented in the form of a state diagram, as shown in Fig. 5. The state diagram is plotted with $a = \gamma_{23}/\gamma_{12}$ on the x axis and $b = \gamma_{31}/\gamma_{12}$ on the y axis. The color represents the angle θ_e that is enclosed between the tangents drawn at the three phase contact point to the fluid 1–fluid 3 and fluid 2–fluid 3 interfaces but defined in fluid 3, as shown in Fig. 2. In general, θ_e increases with an increase in the magnitude of a and/or b .

The state diagram can be broadly divided into four regions. In region 1, $a = b$ but $(a + b) > 1$. Here, fluid 3 always exists as a lens and it is in contact with both fluid 1 and fluid 2. Moreover, the

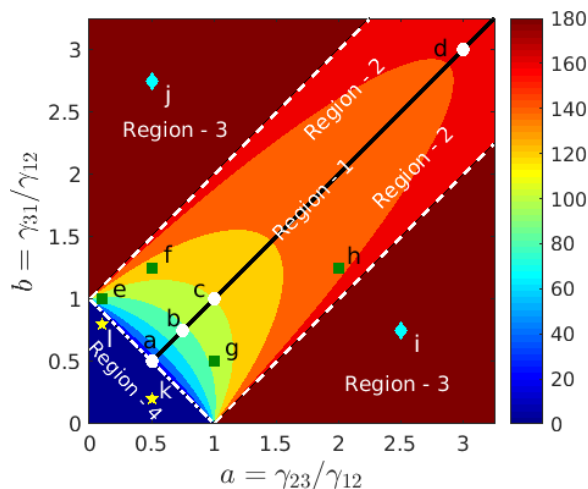


FIG. 5. State diagram classifying the equilibrium configurations of drop of fluid 3 at fluid 1–fluid 2 interface into different regions. The x axis is $a = \gamma_{23}/\gamma_{12}$ and the y axis is $b = \gamma_{31}/\gamma_{12}$. The color bar indicates the equilibrium enclosing angle θ_e . The solid line corresponds to $a = b$, the dashed lines correspond to $b = a + 1$ and $b = a - 1$, and the dot-dashed line corresponds to $a + b = 1$. The equilibrium shapes shown in Figs. 4(a)–4(l) are marked by the corresponding subfigure label in the state diagram.

drop is symmetric. The equilibrium drop shapes corresponding to region 1 are shown in Figs. 4(a)–4(d). As can be inferred from the color bar in Fig. 5, the enclosing angle of the lens θ_e increases with an increase in the value of a (or b). Region 2 occurs both below and above region 1. Region 2 above region 1 is bound by the set of three lines $b = a + 1$, $a + b = 1$, $a = b$, while region 2 below region 1 is bound by $a = b$, $a + b = 1$, $b = a - 1$. In region 2, the drop shape is still a lens in contact with both fluids. However, the lens is not symmetric about the fluid 1–fluid 2 interface. In the region 2 that lies above region 1, the fluid 1–fluid 3 contact area is smaller compared to the fluid 2–fluid 3 contact area, i.e., the drop resides more in fluid 2, as shown in Figs. 4(e) and 4(f). Similarly, in the region 2 that is below region 1, drops reside more in fluid 1, as shown in Figs. 4(g) and 4(h).

In contrast, in region 3 the drop of fluid 3 resides only in one of the fluids and assumes the shape of a circle. In the region 3 lying above region 2 (demarcated by the boundary $b = a + 1$) the drop resides in fluid 2, while in the region 3 below region 2 (demarcated by the boundary $b = a - 1$), the drop resides in fluid 1. Examples of such equilibrium configurations are shown in Figs. 4(i) and 4(j).

In region 4, the drop of fluid 3 placed on the fluid 1–fluid 2 interface spreads completely and takes the shape of a thin film which is symmetric about the fluid 1–fluid 2 interface. This is shown in Figs. 4(k) and 4(l). The boundary $a + b = 1$ demarcates region 4 with other regions in the state diagram. As stated earlier, $S^* \geq 0$ in region 4, while $S^* < 0$ in the other three regions.

Similar phase diagrams have been proposed in the context of preparation and stability of double emulsions [36,37], which concerns two drops of finite volume immersed in a third fluid. In these phase diagrams, different states (completely, partially, or nonengulfing) of a pair of drops are plotted as a function of a and b . It must be noted that such phase diagrams depend upon the amount of fluids present in the system and the physicochemical nature of the stabilizing agents used. Figure 5 is also plotted with a and b as the axes; however, our system deals with a single droplet spreading on an interface of infinite area.

As discussed, the statics of a drop of fluid 3 residing on the fluid 1–fluid 2 interface is very rich, with a plethora of shapes. Since the equilibrium drop shapes are very different in the four regions, the spreading process that leads to these shapes will also be different. In the following section, a detailed investigation of the spreading behavior corresponding to region 1 where $a = b$ and $a + b > 1$ is considered.

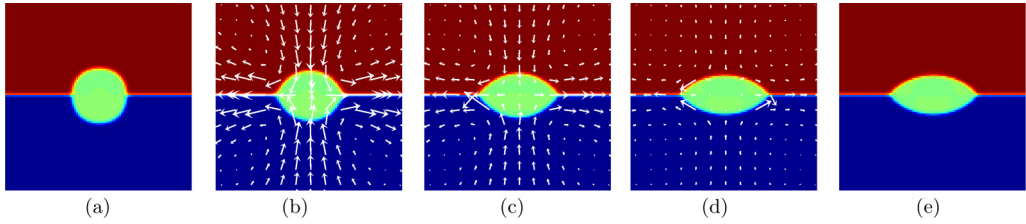


FIG. 6. Shape evolution during symmetric spreading of a drop of fluid 3 placed on a fluid 1–fluid 2 interface, corresponding to the case of $a = b = 0.75$. With time, the drop evolves from the initial configuration of a circle ($t = 0$) to its equilibrium lens shape. The velocity vectors in (b)–(d) show the flow field developed and its consequent decay during the spreading process: (a) $t = 0$, (b) $t = 25\,000$, (c) $t = 75\,000$, (d) $t = 500\,000$, and (e) $t = 1\,000\,000$.

C. Spreading kinetics of drops that form symmetric lens – Region 1

Figure 6 shows the temporal evolution of shape of a drop of fluid 3 placed on fluid 1–fluid 2 interface. The configuration at $t = 0$ is a circular drop, as shown in Fig. 6(a). As time progresses, the drop spreads and correspondingly, the radius $R(t)$ increases while the height $h(t)$ decreases. This spreading process sets up fluid flows both inside the lens and in the outer fluids. Snapshots of this spreading process and the corresponding velocity field at intermediate times are shown in Figs. 6(b)–6(d). It is evident that after the initial transients, the flow field decays as spreading progresses. Beyond time $t = 2 \times 10^5$, the fluid flow ceases, the drop does not spread further, and it takes the final shape corresponding to equilibrium, which is shown in Fig. 6(e). The drop continues to maintain the symmetry about the fluid 1–fluid 2 interface throughout the temporal evolution. Since the density and viscosity of all three fluids are considered to be the same, the spreading process shown in Fig. 6 is solely driven by surface tension forces.

The spreading process that was qualitatively described in Fig. 6 is further quantified in terms of time evolution of radius [Fig. 7(a)], height [Fig. 7(b)], and the enclosing angle [Fig. 7(c)] of the lens for various surface tension values such that $a = b$ is maintained. The radius of the lens plotted in Fig. 7(a) and the height of the lens plotted in Fig. 7(b) are normalized with the initial radius (R_i) and initial height (h_i) of the drop, respectively. Note that the axes of all the plots are in logarithmic scale.

As shown in Fig. 7(a), the radius $R(t)$ monotonically increases with time as expected and finally reaches a plateau, except for the case of $a = b = 0.5$. The latter corresponds to the spreading of

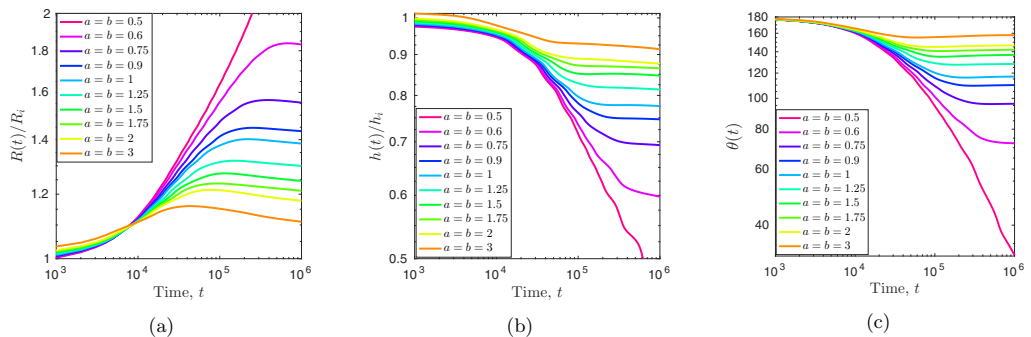


FIG. 7. The time evolution of the geometrical parameters characterizing the kinetics of symmetrically spreading ($a = b$) drops for $a = 0.5$ –3. (a) The radius of the lens $R(t)$ normalized with the initial drop radius R_i is plotted against time. (b) The height of the lens $h(t)$ normalized with the initial drop height h_i (which is the same as R_i) is plotted against time. (c) The enclosing angle of the lens $\theta(t)$ is plotted against time.

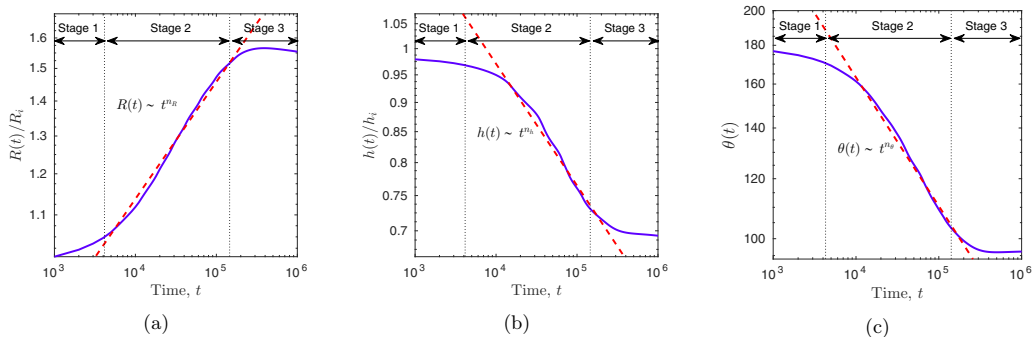


FIG. 8. The classification of kinetics of symmetrically spreading behavior into slow (stage 1 and stage 3) and fast (stage 2) spreading regimes, wherein (a) the normalized radius, (b) the normalized height, and (c) the enclosing angle are plotted against time for the case of $a = b = 0.75$. The dashed lines in each figure indicate the power law fits to the spreading kinetics data in stage 2.

the drop to a thin film while in other cases, the drops evolve into a lenslike shape. The equilibrium radius of the lens decreases with increase in the magnitude of a (or b). It is interesting to note that although the rate of spreading $[dR(t)/dt]$ decreases with increase in the value of a (or b), the lens approaches equilibrium at an earlier time. The normalized height $h(t)/h_i$ shown in Fig. 7(b) and the enclosing angle $\theta(t)$ shown in Fig. 7(c) decrease with time as the spreading proceeds. The plateau in the plots (except for the case $a = b = 0.5$) corresponds to the equilibrium configuration of the drops. The rate of spreading [quantified by $dh(t)/dt$ and $d\theta(t)/dt$] is smaller and therefore, the height and enclosing angle corresponding to the final state of the drops are higher for higher values of a (or b). This behavior is consistent with the observations presented in Fig. 7(a).

To unearth the scaling behavior of the data presented in Fig. 7, further analysis of the spreading behavior is carried out by considering a typical case, say, $a = b = 0.75$. For this case, the radius, height, and enclosing angle of the lens are plotted as a function of time as shown in Figs. 8(a), 8(b) and 8(c), respectively. It is evident that the evolution of the different geometrical parameters during the spreading of a circular-shaped fluid 3 drop placed on the fluid 1–fluid 2 interface broadly consists of three distinct stages, referred to as stage 1, 2, and 3. The time window corresponding to stage 2 is the longest, meaning that a significant spreading of the drop occurs in this time frame. Moreover, $dR(t)/dt$, $dh(t)/dt$, and $d\theta(t)/dt$ in this stage are highest. In stage 1 which precedes stage 2, and in stage 3 which succeeds stage 2, the rate of increase in the radius of the lens (the rate of decrease in the height and the enclosing angle) with respect to time is slower. Stage 1 represents the slow approach of the circular drop to the lenslike shape, indicating the onset of stage 2. It must be noted that the kinetics of spreading in stage 1 is similar and is almost independent of a (or b). The slow spreading in stage 3 represents the exponential relaxation of the spreading lens to its equilibrium configuration [38]. This three stage description is generic for all the cases considered in Fig. 7 except for $a = b = 0.5$, in which case the drop spreads as a thin film. The extent of spreading depends upon the domain size in this case, and therefore stage 3 is absent during the time frame of the simulation. For the purpose of analysis, an $\sim 5\%$ change in the radius of the lens from its initial radius is considered as the onset of stage 2. Similarly, the end of stage 2 and onset of stage 3 is assumed to occur when the radius of the lens becomes $\sim 95\%$ of the radius of the fluid 3 lens at equilibrium.

As the majority of the spreading occurs in stage 2, we further analyze the spreading kinetics in this stage and present a comparison of the data corresponding to various values of a (or b). The spreading behavior in stage 2 can be well approximated with a straight line in the log-log plots shown in Figs. 8(a)–8(c). In other words, in stage 2, $R(t) \sim t^{n_R}$, $h(t) \sim t^{n_h}$, and $\theta(t) \sim t^{n_\theta}$. If a circular drop with $\theta_e = 180^\circ$ is considered it does not evolve from the initial state, which thus

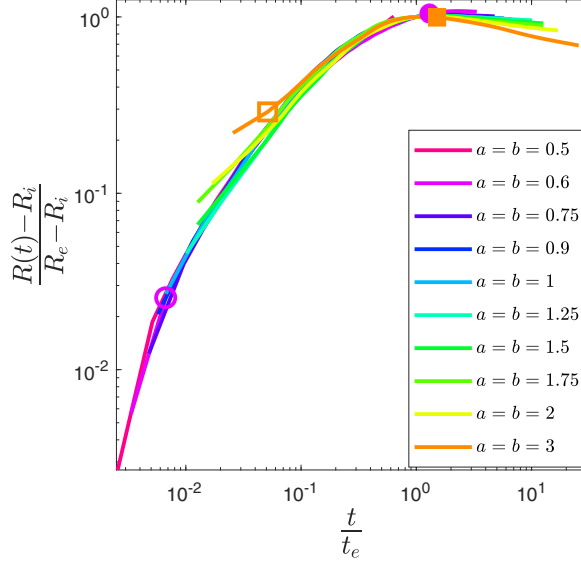


FIG. 9. Data presented in Fig. 7(a) collapse onto a master curve when the x axis is rescaled as t/t_e and the y axis as $\frac{R(t)-R_i}{R_e-R_i}$. Here R_i denotes the initial radius of the drop and R_e denotes the maximum radius that the drop attains at time t_e in stage 3. The onset (open symbol) and the end (filled symbol) of stage 2 for $a = b = 0.6$ and $a = b = 3$ are shown respectively with circle and square symbols.

corresponds to $n_R = n_h = n_\theta = 0$. It was observed that n_R decreases with increase in θ_e , and both n_h and n_θ increase with increase in θ_e . In our simulations, we obtain a thin drop with a small enclosing angle for the case of $a = b = 0.5$, and the power law exponent extracted from simulations is $n_R = 0.1821$, which is close to the predictions of the scaling analysis, $n_R = \frac{1}{6}$, presented in Sec. II C. Another feature that is worth noting is that $n_R = -n_h$ for all values of θ_e , as the two length scales $R(t)$ and $h(t)$ associated with spreading are constrained by the conservation of drop area as shown in Sec. II C. Similarly, as the enclosing angle $\theta(t)$ is related to the ratio of the two length scales $R(t)$ and $h(t)$, $n_\theta \approx n_R - n_h$. Therefore characterizing the temporal evolution of any one length scale or the enclosing angle will suffice in describing the spreading of drops. However, the power law spans over less than a decade in several cases and the measured exponents show a strong dependence on S^* indicating that a small change in surface tension of any of the fluids will result in a large change in the exponent.

We now present an alternative analysis accounting for kinetics of spreading in all three stages. The spreading kinetics, both in experiments and in theory, is often represented by power law behavior as discussed so far, for example, $R(t) \sim t^{n_R}$. These exponents can be used to rescale the data to obtain a master curve, although limited to stage 2 kinetics. However, the general trend, i.e., the similarity of the kinetics of spreading in stages 1–3, can be exploited to obtain a master curve which is independent of the value of a and b . To this end, we replot the data presented in Fig. 7(a) by rescaling the x axis as t/t_e and the y axis as $\frac{R(t)-R_i}{R_e-R_i}$. Here R_i denotes the initial radius of the drop and R_e denotes the maximum radius that the drop attains at time t_e , which occurs in stage 3. The time, t_e , corresponds to the time at which radius reaches a maximum during the spreading process. The maximum occurs due to slight inertia associated with the spreading drop; otherwise it marks the end of the spreading process. The proposed rescaling leads to a collapse of the data shown in Fig. 7(a) into a master curve shown in Fig. 9. This collapse clearly shows that the spreading of drops for various combinations of a (or b) is governed by the same physics. Moreover, it may be noted that the duration of existence of stage 2 kinetics strongly depends on the value of a (or b) or equivalently, on the equilibrium enclosing angle θ_e . As the equilibrium enclosing angle increases,

the duration of stage 2 kinetics progressively decreases. To make this point clear, the onset and end of stage 2 are marked as open and closed symbols in Fig. 9 for $a = b = 0.6$ (denoted by circle) and $a = b = 3$ (denoted by square). The progressive decrease in the duration of stage 2 kinetics with increase in value of a (or b) mentioned above is linked to the fact that the drop approaches the equilibrium enclosing angle at an earlier time. Therefore there is not enough time for the spreading behavior in stage 2 to develop into $\frac{1}{6}$ th kinetics for systems with larger values of a and b , and hence they show an exponent smaller than $\frac{1}{6}$, with the spreading exponent monotonically decreasing with increase in θ_e . However, the spreading kinetics for $a = b = 0.5$ follows $n_R \approx \frac{1}{6}$, since spreading conditions closely match with the assumptions made in deriving the power law scaling. Considering that the duration of the drop spreading in stage 2 is a strong function of a and b , which results in an equilibrium enclosing angle dependent power law exponent, caution should be exercised in the quest for a universal power law scaling.

IV. CONCLUSIONS

In this work, a quantitative study of the statics and kinetics of spreading of a fluid drop on a fluid-fluid interface is carried out using numerical simulations in two dimensions. The kinetics of spreading is characterized in terms of the evolution of geometric parameters such as radius, height, and enclosing angle of the liquid lens. A state diagram corresponding to the equilibrium shapes of the fluid drop is constructed in terms of a and b , which are the scaled interfacial tensions of the fluids. The state diagram can be conveniently divided into four regions: (i) region 1 of symmetric lenses, wherein the contact area of fluid 3 with fluid 1 and fluid 2 is the same; (ii) region 2 of asymmetric lenses, wherein the fluid 3 shares different contact areas with fluid 1 and fluid 2; (iii) region 3, corresponding to circular drops residing in either fluid 1 or fluid 2; and (iv) region 4, where fluid 3 exists as a thin film at the fluid 1–fluid 2 interface.

Further, a detailed analysis of the temporal evolution of the spreading of fluid 3 at the fluid 1–fluid 2 interface corresponding to $a = b$ and $a + b \geq 1$ is conducted. In this region, fluid 3 spreads as a symmetric lens leading to the equilibrium shapes depicted in region 1 in the state diagram. All the geometrical parameters that characterize the spreading process are found to follow a power law behavior. The power law exponents are found to exhibit a linear and strong exponential-like dependency with respect to the equilibrium enclosing angle and the normalized spreading coefficient, respectively. The strong dependence of the scaling exponents on the equilibrium enclosing angle and the normalized spreading coefficient demands that caution should be exercised in ascertaining the universality of the spreading behavior. Moreover, we have presented a master curve which collapses the spreading kinetics data corresponding to different equilibrium enclosing angles. Our results will serve as benchmark to compare the spreading behavior in other regimes, namely, regions 2, 3, and 4, as well as in the presence of other effects such as inertia, gravity, influence of additives (surfactant, salt, etc.), fluid miscibility, and reactivity.

-
- [1] A. Z. Stetten, S. V. Iasella, T. E. Corcoran, S. Garoff, T. M. Przybycien, and R. D. Tilton, Surfactant-induced Marangoni transport of lipids and therapeutics within the lung, *Curr. Opin. Colloid Interface Sci.* **36**, 58 (2018).
 - [2] K. Mishra, D. Van den Ende, and F. Mugele, Recent developments in optofluidic lens technology, *Micromachines* **7**, 102 (2016).
 - [3] P. K. Sangu, V. M. Kumar, M. S. Shekhar, M. K. Chagam, P. P. Goli, and P. K. Tirupati, A study on Tailabindu Pariksha—An ancient ayurvedic method of urine examination as a diagnostic and prognostic tool, *Ayu* **32**, 76 (2011).
 - [4] A. C. Kar, R. Sharma, B. K. Panda, and V. P. Singh, A study on the method of Taila Bindu Pariksha (oil drop test), *Ayu* **33**, 396 (2012).

- [5] D. P. Hoult, Oil spreading on the sea, *Annu. Rev. Fluid Mech.* **4**, 341 (1972).
- [6] J. F. Joanny, Wetting of a liquid substrate, *Physicochem. Hydrodyn.* **9**, 183 (1987).
- [7] S. Berg, Marangoni-driven spreading along liquid-liquid interfaces, *Phys. Fluids* **21**, 032105 (2009).
- [8] G. Karapetsas, R. V. Craster, and O. K. Matar, Surfactant-driven dynamics of liquid lenses, *Phys. Fluids* **23**, 122106 (2011).
- [9] W. R. C. Phillips, On the spreading radius of surface tension driven oil on deep water, *Appl. Sci. Res.* **57**, 67 (1996).
- [10] M. Foda and R. G. Cox, The spreading of thin liquid films on a water-air interface, *J. Fluid Mech.* **101**, 33 (1980).
- [11] J. A. Fay, The spread of oil slicks on a calm sea, in *Oil on the Sea* (Springer, New York, 1969), pp. 53–63.
- [12] R. Chebbi, Spreading of oil on water in the surface-tension regime, *Environ. Fluid Mech.* **14**, 1443 (2014).
- [13] J. G. E. M. Fraaije and A. M. Cazabat, Dynamics of spreading on a liquid substrate, *J. Colloid Interface Sci.* **133**, 452 (1989).
- [14] C. Huh, M. Inoue, and S. G. Mason, Uni-directional spreading of one liquid on the surface of another, *Can. J. Chem. Eng.* **53**, 367 (1975).
- [15] D. W. Camp and J. C. Berg, The spreading of oil on water in the surface-tension regime, *J. Fluid Mech.* **184**, 445 (1987).
- [16] V. Bergeron and D. Langevin, Monolayer Spreading of Polydimethylsiloxane Oil on Surfactant Solutions, *Phys. Rev. Lett.* **76**, 3152 (1996).
- [17] A. D. Dussaud and S. M. Troian, Dynamics of spontaneous spreading with evaporation on a deep fluid layer, *Phys. Fluids* **10**, 23 (1998).
- [18] M. Santiago-Rosanne, M. Vignes-Adler, and M. G. Velarde, On the spreading of partially miscible liquids, *J. Colloid Interface Sci.* **234**, 375 (2001).
- [19] R. Dandekar, A. Pant, and B. A. Puthenveetil, Film spreading from a miscible drop on a deep liquid layer, *J. Fluid Mech.* **829**, 304 (2017).
- [20] P.-G. De Gennes, F. Brochard-Wyart, and D. Quéré, *Capillarity and Wetting Phenomena: Drops, Bubbles, Pearls, Waves* (Springer Science & Business Media, New York, 2013).
- [21] R. V. Craster and O. K. Matar, On the dynamics of liquid lenses, *J. Colloid Interface Sci.* **303**, 503 (2006).
- [22] N. D. D. I. Pietro and R. G. Cox, The spreading of a very viscous liquid on a quiescent water surface, *Q. J. Mech. Appl. Math.* **32**, 355 (1979).
- [23] D. M. Anderson, G. B. McFadden, and A. A. Wheeler, Diffuse-interface methods in fluid mechanics, *Annu. Rev. Fluid Mech.* **30**, 139 (1998).
- [24] C. Semperebon, T. Krüger, and H. Kusumaatmaja, Ternary free-energy lattice Boltzmann model with tunable surface tensions and contact angles, *Phys. Rev. E* **93**, 033305 (2016).
- [25] N. Bala, M. Pepona, I. Karlin, H. Kusumaatmaja, and C. Semperebon, Wetting boundaries for a ternary high-density-ratio lattice Boltzmann method, *Phys. Rev. E* **100**, 013308 (2019).
- [26] V. M. Kendon, M. E. Cates, I. Pagonabarraga, J.-C. Desplat, and P. Bladon, Inertial effects in three-dimensional spinodal decomposition of a symmetric binary fluid mixture: A lattice Boltzmann study, *J. Fluid Mech.* **440**, 147 (2001).
- [27] P. M. Chaikin, T. C. Lubensky, and T. A. Witten, *Principles of Condensed Matter Physics* (Cambridge University Press, Cambridge, England, 1995), Vol. 10.
- [28] E. Orlandini, M. R. Swift, and J. M. Yeomans, A lattice Boltzmann model of binary-fluid mixtures, *Europhys. Lett.* **32**, 463 (1995).
- [29] C. K. Batchelor and G. K. Batchelor, *An Introduction to Fluid Dynamics* (Cambridge University Press, Cambridge, England, 2000).
- [30] T. Krüger, H. Kusumaatmaja, A. Kuzmin, O. Shardt, G. Silva, and E. M. Viggen, *The Lattice Boltzmann Method* (Springer, New York, 2017), Vol. 10, p. 978.
- [31] S. P. Thampi, I. Pagonabarraga, and R. Adhikari, Lattice-Boltzmann-Langevin simulations of binary mixtures, *Phys. Rev. E* **84**, 046709 (2011).
- [32] A. Tiribocchi, N. Stella, G. Gonnella, and A. Lamura, Hybrid lattice Boltzmann model for binary fluid mixtures, *Phys. Rev. E* **80**, 026701 (2009).

- [33] J.-C. Desplat, I. Pagonabarraga, and P. Bladon, Ludwig: A parallel lattice-Boltzmann code for complex fluids, [Comput. Phys. Commun.](#) **134**, 273 (2001).
- [34] M. Bernaschi, S. Melchionna, and S. Succi, Mesoscopic simulations at the physics-chemistry-biology interface, [Rev. Mod. Phys.](#) **91**, 025004 (2019).
- [35] W. D. Harkins and A. Feldman, Films. The spreading of liquids and the spreading coefficient, [J. Am. Chem. Soc.](#) **44**, 2665 (1922).
- [36] J. Guzowski, P. M. Korczyk, S. Jakiela, and P. Garstecki, The structure and stability of multiple microdroplets, [Soft Matter](#) **8**, 7269 (2012).
- [37] N. Wang, C. Semperebon, H. Liu, C. Zhang, and H. Kusumaatmaja, Modelling double emulsion formation in planar flow-focusing microchannels, [J. Fluid Mech.](#) **895**, A22 (2020).
- [38] S. P. Thampi, I. Pagonabarraga, R. Adhikari, and R. Govindarajan, Universal evolution of a viscous-capillary spreading drop, [Soft Matter](#) **12**, 6073 (2016).